Genetic diagnosis of Mendelian disorders via RNA sequencing

Laura S Kremer[1,2,21], Daniel M Bader[3,4,21], Christian Mertes[3], Robert Kopajtich[1,2], Garwin Pichler[5], Arcangela Iuso[1,2], Tobias B Haack[1,2], Elisabeth Graf[1,2], Thomas Schwarzmayr[1,2], Caterina Terrile[1], Eliška Koňaříková[1,2], Birgit Repp[1,2], Gabi Kastenmüller[6], Jerzy Adamski[7], Peter Lichtner[1], Christoph Leonhardt[8], Benoit Funalot[9], Alice Donati[10], Valeria Tiranti[11], Anne Lombes[12,13,14], Claude Jardel[12,15], Dieter Gläser[16], Robert W. Taylor[17], Daniele Ghezzi[9], Johannes A Mayr[18], Agnes Rötig[8], Peter Freisinger[19], Felix Distelmaier[20], Tim M Strom[1,2], Thomas Meitinger[1,2], Julien Gagneur[3], Holger Prokisch[1,2,*].

1. Institute of Human Genetics, Helmholtz Zentrum München, 85764 Neuherberg, Germany
2. Institute of Human Genetics, Klinikum rechts der Isar, Technische Universität München, , 81675 München, Germany
3. Department of Informatics, Technische Universität München, 85748 Garching, Germany
4. Quantitative Biosciences Munich, Gene Center, Department of Biochemistry, Ludwig Maximilian Universität München, 81377 Munich, Germany
5. Department of Proteomics and Signal Transduction, Max-Planck Institute of Biochemistry, 82152 Martinsried, Germany
6. Institute of Bioinformatics and Systems Biology, Helmholtz Zentrum München, 85764 Neuherberg, Germany
7. Institute of Experimental Genetics, Genome Analysis Center, Helmholtz Zentrum München, German Research Center for Environmental Health, 85764 Neuherberg, Germany
8. Neuropädiatrie, Neonatologie, 78050 Villingen-Schwenningen, Germany
9. INSERM U1163, Université Paris Descartes - Sorbonne Paris Cité, Institut Imagine, 75015 Paris, France
10. Metabolic Unit, A. Meyer Children's Hospital, Florence, Italy
11. Unit of Molecular Neurogenetics, Foundation IRCCS (Istituto di Ricovero e Cura a Carettere Scientifico) Neurological Institute “Carlo Besta”, 20126 Milan, Italy
12. Inserm UMR 1016, Institut Cochin, 75014 Paris, France
13. CNRS UMR 8104, Institut Cochin, 75014 Paris, France
14. Université Paris V René Descartes, Institut Cochin, 75014 Paris, France
15. AP/HP, GHU Pitié-Salpêtrière, Service de Biochimie Métabolique, 75013, Paris, France
16. Genetikum, Genetic Counseling and Diagnostics, 89231 Neu-Ulm, Germany
17. Wellcome Trust Centre for Mitochondrial Research, Institute of Neuroscience, Newcastle University, Newcastle upon Tyne, NE2 4HH, UK
18. Department of Pediatrics, Paracelsus Medical University, A-5020 Salzburg, Austria
19. Department of Pediatrics, Klinikum Reutlingen, 72764 Reutlingen, Germany
20. Department of General Pediatrics, Neonatology and Pediatric Cardiology, University Children's Hospital, Heinrich-Heine-University Düsseldorf, 40225 Düsseldorf, Germany
21. These authors contributed equally to this work.

Correspondence should be addressed to Holger Prokisch (prokisch@helmholtz-muenchen.de) or Julien Gagneur (gagneur@in.tum.de).

Abstract

Across a large variety of Mendelian disorders, 50 to 75% of undiagnosed patients do not receive a genetic diagnosis by whole exome sequencing indicative of underlying regulatory variants. In contrast, whole genome sequencing allows the discovery of all genetic variants, but their significant number, coupled with a poor understanding of the non-coding genome, makes their prioritization challenging. Here, we demonstrate the power of directly sequencing transcriptomes by providing a genetic diagnosis for 11% (5 of 47) of unsolved mitochondrial disease patients and strong candidates for other patients. We found a median of 1 aberrantly expressed gene, 5 aberrant splicing events, and 6 mono-allelically expressed rare variants in patient-derived fibroblasts and established disease-causing roles for each kind. Private exons often arose from sites that are weakly spliced in other individuals, providing an important clue for future variant prioritization. One such intronic exon-creating variant was found in three unrelated families in the complex I assembly factor TIMMDC1, which we consequently established as a novel disease-associated gene. In conclusion, our study expands the diagnostic tools for detecting non-exonic variants of Mendelian disorders and provides examples of intronic loss-of-function variants with pathological relevance.

To investigate RNA sequencing (RNA-seq) as a diagnostic tool for Mendelian disorders, we considered mitochondrial disorders for three reasons. First, mitochondrial disorders represents the most frequent inborn errors of metabolism affecting 1 in 4,300 birth[1]. Second, the genetic basis is large with causative defects identified in approximately 300 genes and a presumably large number of additional disease-associated genes still awaiting identification[2]. Third, for the majority of patients, disease mechanisms can be assayed in dermal fibroblasts even though the disease may manifest in different tissues[3]. This allows rapid demonstration of the necessary and sufficient role of candidate variants by complementation assays[4]. It also indicates that disease-causing expression defects, if any, should be detectable in these cells.

We selected 105 patient fibroblast cell lines, 47 from cases without genetic diagnosis. These patients serve as good controls for each other, since, as for other rare disorders, it is unlikely that many share a single genetic cause. RNA-seq identified 12,680 transcribed genes across all samples (Online Methods). We systematically searched for three possible causes for the rare disorder: i) genes with aberrant expression level[5–7], ii) genes with aberrant splicing[8] and iii) mono-allelic expression of rare variants[9] (**Fig. 1**). Once normalized for technical biases, sex, and biopsy site (**Supplementary Fig. 1**), the samples typically presented few aberrantly expressed genes (median of 1, **Fig. 2a**) with unusually large (|Z-score| > 3) and significant differential expression (Hochberg adjusted *P*-value < 0.05). When searching for aberrantly expressed genes encoding mitochondrial proteins, we found *MGST1* in one and *TIMMDC1* in two samples, significantly reduced (**Fig. 2b-d** and **Supplementary Fig. 2)**. For both genes, no variant was reported to be disease-associated and no case of potential bi-allelic rare variant is listed in our in-house database comprising more than 1,200 whole-exomes from mitochondriopathy patients and from 10,000 controls. To evaluate the consequences of reduced RNA expression on the protein level we performed quantitative proteomics from a second aliquot of cells taken at the same time as the transcript aliquot in a total number of 31 patients. With 2% remaining of MGST1 and lack

of detection of TIMMDC1 in the respective samples, the quantification unraveled an even stronger effect on protein level, indicating a loss of function (**Fig. 2e** and **Supplementary Fig. 3**). MGST1, a microsomal glutathione S-transferase, is involved in the oxidative stress defense[10]. Consequently, the loss of expression of MGST1 is a likely cause of the disease of the patient, who suffers from an infantile-onset neurodegenerative disorder similar to a recently published case with another defect in the reactive oxygen species (ROS) defense system (**Supplementary Information**)[11], but also suggested a treatment with antioxidants. Both TIMMDC1 patients presented with muscular hypotonia, developmental delay and neurological deterioration leading to death in the first 3 years of life (**Supplementary Information**). Consistent with the described function of TIMMDC1 as a respiratory chain complex I assembly factor[12,13], we found isolated complex I deficiency in muscle (**Supplementary Fig. 2**), and globally decreased levels of complex I subunits in fibroblasts by quantitative proteomics (**Fig. 2e** and **Supplementary Fig. 2**) and western blot (**Fig. 2f).** Re-expression of *TIMMDC1* in these cells increased complex I subunit levels (**Fig. 2f**). These results not only validate TIMMDC1-deficiency as disease causing but also provide compelling evidence for an important function of TIMMDC1 in complex I assembly.

We identified aberrant splicing events by testing for differential splicing in each patient against all others using an annotation-free algorithm to detect splice sites (Online Methods, median of 5 abnormal events per sample, **Fig. 3a**). Among the 173 aberrant splicing events detected in the undiagnosed patients, the most abundant events were, apart from differential expression of isoforms, exon skipping followed by the creation of new exons (**Fig. 3b).** Two genes encoding mitochondrial proteins, *TIMMDC1* and *CLPP*, were among the 10 most significant genes (**Supplementary Table 1**). Out of 136 exon-junction reads overlapping the acceptor site of *CLPP* exon 6 for patient #58955, 82 (percent spliced in Ψ = 60%) skipped exon 5, and 14 (Ψ =10%) showed a 3'-truncated exon 5, in striking contrast to other samples (**Fig. 3c**). The likely genetic cause of these two splice defects is a rare homozygous variant (c.661G>A, 1.2×10^{-5} frequency in the ExAC[14] of the last nucleotide of exon 5 uniquely found in this patient (**Supplementary Fig. 4**). Both splice defects are predicted to result in truncated CLPP and western blots corroborated the complete loss of full-length CLPP (**Supplementary Fig. 4**). *CLPP* codes for a mitochondrial ATP-dependent endopeptidase[15]. CLPP-deficiency causes Perrault-syndrom[16,17] resembling the clinical presentation of the patient including microcephaly, deafness, and severe psychomotor retardation confirming the molecular diagnosis (**Supplementary Information**).

Split read distribution indicated that both TIMMDC1-deficiency patients expressed almost exclusively a *TIMMDC1* isoform with a new exon in intron 5 (**Fig. 3d**). This new exon introduces a frameshift yielding a premature stop codon (p.Gly199_Thr200ins5*, **Fig. 3e**). Moreover, this new exon contained a rare variant (c.596+2146A>G) not listed in The 1000 Genomes Project[18,19]. Whole genome sequencing (WGS) demonstrated that this variant is homozygous in both patients (**Fig. 3e**). WGS of 60 further pediatric cases revealed an additional family with three affected siblings and similar clinical symptoms carrying the same homozygous intronic variant (**Fig. 3e**, **Supplementary Fig. 2**). Two siblings died before the age of 10 years. The younger brother (#96687), now 6 years, presented, similar to the patients described above, with muscle hypotonia, failure to thrive and neurological impairment (**Supplementary Information**). Western blot analysis confirmed TIMMDC1-deficiency (**Fig. 2f**) and impaired complex I assembly which was restored after re-expression of *TIMMDC1* (**Fig. 2g**). The

discovery of the same intronic *TIMMDC1* variant in three unrelated families from three different ethnicities convincingly demonstrated the causality of this variant for the TIMMDC1 loss-of-function.

In almost all non-TIMMDC1-deficiency samples, we noticed a few split reads supporting inclusion of the new exon (**Fig. 3d**), consistent with an earlier report that many cryptic splice sites are not entirely repressed but active at low levels[20]. Splicing defects are increasingly recognized to play a major role in Mendelian[21] and common disorders[8]. We set out to quantify this phenomenon and to ask how frequent private exons originate from weakly spliced exons, independently of their possible association with disease. Therefore, we modeled the distribution of Ψ for the 1,603,042 splicing events detected genome-wide in 105 samples as a mixture of three components. This classified splicing frequencies per splice site as strong (20%, $\Psi > 0.053$), weak (16% $< \Psi <$), or background (64%, $\Psi < 0.0016$, Online Methods, **Fig. 3f** and **Supplementary Fig. 5**). Strikingly, the majority (70%) of the 30 private exons we discovered originated from weak splice sites (**Fig. 3f bottom**). Our finding shows that weakly spliced cryptic exons are loci more susceptible to turn into strongly spliced sites than other intronic regions. Hence, these results suggest that the prioritization of deep intronic variants of unknown significances gained through WGS could be improved by annotating weak splice sites and their resulting cryptic exon.

As a third approach to discover regulatory variants, we searched for mono-allelic expression (MAE) of rare variants. Out of 35,521 heterozygous SNVs detected by WES, 7,622 were sufficiently covered by RNA-seq to call MAE (more than 10 reads), 20 showed MAE of which 6 were rare (numbers as median per patient, **Fig. 4a**). One patient (#80256) showing significant mono-allelic expression of a rare SNV of unknown significance in *ALDH18A1* (c.1864C>T, p.Arg622Trp), encoding an enzyme involved in mitochondrial proline metabolism[22,23], was compound heterozygous with a nonsense variant (c.1988C>A, p.Ser663*****) (**Fig. 4b** and **Supplementary Fig. 6**). Since the clinical presentation of the patient was not consistent with reported ALDH18A1-deficiency cases, the patient had remained without diagnosis. Although the detected allele was expressed at its normal level, the quantitative proteome investigation showed severe reduction down to 2% of ALDH18A1 (**Fig. 4c**), indicating that the rare variant may affect translation or protein stability. Metabolomics profile of blood plasma was in accordance with a defect in proline metabolism (**Fig. 4d**) and the following changes in urea cycle. Patient fibroblasts showed a growth defect that was rescued by supplementation of proline, validating impaired proline metabolism as disease cause (**Fig. 4e**). In another patient (#62346) with two mutations in *MCOLN1* (c.681-19A>C, p.Lys227_Leu228ins16* and c.832C>T, p.Gln278*), we found MAE of the intronic variant. The allele with the nonsense mutation was not detected, most likely due to nonsense-mediated decay. In contrast, the intronic variant was detected at low levels expressed as part of a retained intron, which introduced a nonsense codon (**Fig. 4f** and **Supplementary Fig. 7**). Mutations in *MCOLN1* are associated with mucolipidosis[24], which resembles the clinical presentation of the patient (**Supplementary information**) and established the genetic diagnosis.

Altogether, our study demonstrates the power of RNA sequencing in combination with stringent filter criteria for genetic diagnosis by discovering a new disease-associated gene, by providing a diagnosis for 11% (5 of 47) of unsolved cases, and by identifying strong candidates for other patients (**Fig 5a**). To our surprise, most identified variants are intronic, affected splicing and

caused loss of function (**Fig 5b**). We further show that private exons often arise from loci with weak splicing of about 1%. We use fibroblast cell lines since the disease-affected tissue was not available, which is typical in clinical practice. Non-affected tissues have the advantage that the regulatory consequences on other genes are limited and therefore the causal defects are more likely to stand out as outliers[25]. In conclusion, we foresee RNA sequencing as an essential companion of genome sequencing to address unsolved cases.

References

1. Skladal, D., Halliday, J. & Thorburn, D. R. Minimum birth prevalence of mitochondrial respiratory chain disorders in children. *Brain* **126,** 1905–1912 (2003).

2. Mayr, J. A. *et al.* Spectrum of combined respiratory chain defects. *J. Inherit. Metab. Dis.* **38,** 629–640 (2015).

3. Haack, T. B. *et al.* ELAC2 mutations cause a mitochondrial RNA processing defect associated with hypertrophic cardiomyopathy. *Am. J. Hum. Genet.* **93,** 211–223 (2013).

4. Haack, T. B. *et al.* Exome sequencing identifies ACAD9 mutations as a cause of complex I deficiency. *Nat. Genet.* **42,** 1131–4 (2010).

5. Zeng, Y. *et al.* Aberrant Gene Expression in Humans. *PLoS Genet.* **11,** 1–20 (2015).

6. Zhao, J. *et al.* A Burden of Rare Variants Associated with Extremes of Gene Expression in Human Peripheral Blood. *Am. J. Hum. Genet.* **98,** 299–309 (2016).

7. Guan, J. *et al.* Exploiting aberrant mRNA expression in autism for gene discovery and diagnosis. *Hum. Genet.* **135,** 1–15 (2016).

8. Li, Y. I. *et al.* RNA splicing is a primary link between genetic variation and disease. *Science* **352,** 600–4 (2016).

9. Albers, C. a *et al.* Compound inheritance of a low-frequency regulatory SNP and a rare null mutation in exon-junction complex subunit RBM8A causes TAR syndrome. *Nat. Genet.* **44,** 435–439 (2012).

10. Lee, K. K., Shimoji, M., Hossain, Q. S., Sunakawa, H. & Aniya, Y. Novel function of glutathione transferase in rat liver mitochondrial membrane: role for cytochrome c release from mitochondria. *Toxicol. Appl. Pharmacol.* **232,** 109–18 (2008).

11. Holzerova, E. *et al.* Human thioredoxin 2 deficiency impairs mitochondrial redox homeostasis and causes early-onset neurodegeneration. *Brain* **139,** 346–354 (2015).

12. Guarani, V. *et al.* TIMMDC1/C3orf1 Functions as a Membrane-Embedded Mitochondrial Complex I Assembly Factor through Association with the MCIA Complex. *Mol. Cell.*

Biol. **34,** 847–861 (2014).

13. Andrews, B., Carroll, J., Ding, S., Fearnley, I. M. & Walker, J. E. Assembly factors for the membrane arm of human complex I. *Proc. Natl. Acad. Sci. U. S. A.* **110,** 18934–9 (2013).

14. Exome Aggregation Consortium *et al. Analysis of protein-coding genetic variation in 60,706 humans. bioRxiv* (Cold Spring Harbor Labs Journals, 2015). doi:10.1101/030338

15. Halperin, T., Zheng, B., Itzhaki, H., Clarke, A. K. & Adam, Z. Plant mitochondria contain proteolytic and regulatory subunits of the ATP-dependent Clp protease. *Plant Mol. Biol.* **45,** 461–468 (2001).

16. Jenkinson, E. M. *et al.* Perrault Syndrome Is Caused by Recessive Mutations in CLPP, Encoding a Mitochondrial ATP-Dependent Chambered Protease. *Am. J. Hum. Genet.* **92,** 605–613 (2013).

17. Jenkinson, E. M. *et al.* Perrault syndrome: further evidence for genetic heterogeneity. *J. Neurol.* **259,** 974–976 (2012).

18. Sudmant, P. H. *et al.* An integrated map of structural variation in 2,504 human genomes. *Nature* **526,** 75–81 (2015).

19. Auton, A. *et al.* A global reference for human genetic variation. *Nature* **526,** 68–74 (2015).

20. Kapustin, Y. *et al.* Cryptic splice sites and split genes. *Nucleic Acids Res.* **39,** 5837–44 (2011).

21. Sibley, C. R., Blazquez, L. & Ule, J. Lessons from non-canonical splicing. *Nat. Rev. Genet.* **17,** 407–421 (2016).

22. Adams, E. & Frank, L. Metabolism of Proline and the Hydroxyprolines. *Annu. Rev. Biochem.* **49,** 1005–1061 (1980).

23. Baumgartner, M. R. *et al.* Hyperammonemia with reduced ornithine, citrulline, arginine and proline: a new inborn error caused by a mutation in the gene encoding delta(1)-pyrroline-5-carboxylate synthase. *Hum. Mol. Genet.* **9,** 2853–8 (2000).

24. Bach, G. *et al.* Identification of the gene causing mucolipidosis type IV. *Nat. Genet.* **26,** 118–123 (2000).

25. Gagneur, J. *et al.* Genotype-Environment Interactions Reveal Causal Pathways That Mediate Genetic Effects on Phenotype. *PLoS Genet.* **9,** e1003803 (2013).

Methods

Exome sequencing

Exome sequencing was essentially performed as described previously[1]. In brief, exonic regions were enriched using the SureSelect Human All Exon kit from Agilent (**Supplemental Table 2**) followed by sequencing as 100 bp paired-end runs on a Illumina HiSeq2000 and Illumina HiSeq2500 (AG_50MB_v4 and AG_50MB_v5 exome kit samples) or as 76 bp paired-end runs on the Illumina GAIIx (AG_38MB_v1 and AG_50MB_v3 exome kit samples).

Processing of Exome sequencing files

Read alignment to the human reference genome (UCSC Genome Browser build hg19) was done using Burrows-Wheeler Aligner[2] (v.0.7.5a). Single-nucleotide variants and small insertions and deletions (indels) were detected with SAMtools[3,4](version 0.1.19). Variants with a quality score below 90, a genotype quality below 90, a mapping quality below 30, and a read coverage below 10 were discarded. The reported variants and small indels were annotated with the most severe entry by the Variant Effector Predictor[5] based on The Sequence Ontology term ranking [6]. Variants with a frequency < 0.001 within the ExAC database[7] were defined as rare. Variants within a 5 bp window around a splice site were considered as splice site variants.

Cell culture

Primary patient fibroblast cell lines, normal human dermal fibroblasts (NHDF) from neonatal tissue (Lonza), and 293FT cells (Thermo Fisher Scientific) were cultured in high glucose DMEM (Life Technologies) supplemented with 10% FBS, 1% penicillin/streptomycin, and 200 μM uridine at 37 °C and 5% CO_2. All fibroblast cell lines have been tested negative for mycoplasma contamination.

RNA sequencing

Non-strand specific, polyA-enriched RNA sequencing was performed as described earlier[8]. Briefly, RNA was isolated from whole-cell lysates using the AllPrep RNA Kit (Qiagen) and RNA integrity number (RIN) was determined with the Agilent 2100 BioAnalyzer (RNA 6000 Nano Kit, Agilent). For library preparation, 1 µg of RNA was poly(A) selected, fragmented, and reverse transcribed with the Elute, Prime, Fragment Mix (Illumina). End repair, A-tailing, adaptor ligation, and library enrichment were performed as described in the Low Throughput protocol of the TruSeq RNA Sample Prep Guide (Illumina). RNA libraries were assessed for quality and quantity with the Agilent 2100 BioAnalyzer and the Quant-iT PicoGreen dsDNA Assay Kit (Life Technologies). RNA libraries were sequenced as 100 bp paired-end runs on an Illumina HiSeq2500 platform.

Processing of RNA sequencing files

RNA-seq reads were demultiplexed and mapped with STAR[9] (version 2.4.2a) to the hg19 genome assembly (UCSC Genome Browser build). In addition to the default parameters we

detected gene fusions and increased sensitivity for novel splice junctions (chimSegmentMin=20, twopassMode="Basic"). Analysis was restricted to the 27,682 UCSC Known Genes[10] (genome annotation version hg19) of chromosomes 1 to 22, M, X, or Y. Per gene, reads that are paired with mates from opposite strands and that overlapped completely within the gene on either strand orientation were counted using the *summarizeOverlaps* function of the R/Bioconductor GenomicAlignments[11] package (parameters: mode=intersectionStrict, singleEnd=FALSE, ignore.strand=TRUE, fragments=FALSE). If the 95th percentile of the coverage across all samples was below 10 reads the gene was considered "not expressed" and discarded from later analysis.

Computing RNA fold changes and differential expression

Before testing for differential expression between one patient of interest and all others, we controlled for technical *batch effect*, *sex*, and biopsy site as inferred from the expression of *hox* genes (**Supplementary information**, **Supplementary Table 3**). We modeled the RNA-seq read counts $K_{i,j}$ of gene i in sample j with a generalized linear model using the R/Bioconductor DESeq2 package[12,13]:

$$K_{i,j} \sim NB\left(s_j \times q_{i,j}, \alpha_i\right)$$

$$\log_2(q_{i,j}) = \beta_i^0 + \beta_i^{condition}\mathbf{x}_{i,j}^{condition} + \beta_i^{batch}\mathbf{x}_{i,j}^{batch} + \beta_i^{sex}\mathbf{x}_{i,j}^{sex} + \beta_i^{hox}\mathbf{x}_{i,j}^{hox}$$

Where NB is the negative binomial distribution; α_i is a gene specific dispersion parameter; s_j is the size factor of sample j; β_i^0 is the intercept parameter for gene i. The value of $\mathbf{x}_{i,j}^{condition}$ is 1 for all RNA samples j of the patient of interest, thereby allowing for biological replicates, and 0 otherwise. The resulting vector $\beta_i^{condition}$ represents the $\log_2$-fold changes for one patient against all others. Z-scores were computed by dividing the fold changes by the standard deviation of the normalized expression level of the respective gene. The *P*-values corresponding to the $\beta_i^{condition}$ were corrected for multiple testing using the Hochberg family-wise error rate method[14].

Splicing

The Leafcutter[15] software was utilized to detect aberrant splicing. Each patient was tested against all others. To adjust Leafcutter to the rare disease setting, we modified the parameters to detect rare clusters, capture local gene fusion events and to detect junctions unique to a patient (minclureads=30; maxintronlen=500,000; mincluratio=1e-5, **Supplementary Table 4**). Furthermore, one sample was tested against all other samples (min_samples_per_group=1; min_samples_per_intron=1). The resulting *P*-values were corrected for multiple testing using a family-wise error rate approach[14].

The significant splice events (adjusted *P*-value < 0.05) detected in the undiagnosed patients were visually classified as exon skipping, exon truncation, exon elongation, new exon, complex splicing (any other splicing event or a combination of the aforementioned ones) and false positives.

For further analysis, only reads spanning a splice junction, so called split reads, were extracted with a mapping quality of greater than 10 to reduce the false positive rate due to mapping issues. Each splice site was annotated as belonging to the start or end of a known exon or to be entirely new. For the reference exon annotation the GENCODE release 24 based on GRCh37 was used[16]. The percent spliced in (Ψ) values for the 3' and 5' sites were calculated as described earlier[17]:

$$\psi_5(D,A) = \frac{n(D,A)}{\sum_{A'} n(D,A')} \quad \text{and} \quad \psi_3(D,A) = \frac{n(D,A)}{\sum_{D'} n(D',A)}$$

Where *D* is a donor site and *A* is an acceptor site. *n(D,A)* denotes the number of reads spanning the given junction. *D'* and *A'* represent all possible donor and acceptor sites, respectively.

Classification of splice sites into background, weak and strong was done by modeling the distribution of the ψ_5 and ψ_3-values with three components. Identifiability of the three components was facilitated by considering three groups of junctions depending on previous annotation of splice sites: 'no side is annotated', 'one side is annotated' and 'both sides are annotated'. Specifically, the number of split reads *n(D,A)* of a junction conditioned on the total number of reads $N(D,A) = \sum_{A'} n(D,A')$, for ψ_5, and $N(D,A) = \sum_{D'} n(D',A)$, for ψ_3, was modeled as:

$$P\big(n(D,A)\big|N(D,A)\big) = \sum_{c\in\{bg,wk,st)} \sum_{s=0,1,2} \pi_{s,c}\, BetaBin(n(D,A)|N(D,A),\alpha_c,\beta_c)$$

where *c* is the component index, *s* the number of annotated sites and BetaBin the beta-binomial distribution. Hence, the components were modeled to have the same parameters α_c, β_c in all three groups but their mixing proportions $\pi_{s,c}$ to be group-specific. Fitting was performed using the expectation-maximization algorithm. For the initial step, the data points were classified as background ($\psi < 0.001$), weak spliced ($\psi < 0.1$) and canonical ($\psi >= 0.1$). After convergence of the clustering the obtained parameters were used to estimate the probability for each junction side to belong to a given class.

Detection of Mono-allelic expression

For mono-allelic expression analysis only heterozygous single nucleotide variants with only one alternative allele detected from exome sequencing data were used. The same quality filters were used as mentioned in the exome sequencing part, but no frequency filter was applied. To get allele counts from RNA sequencing for the remaining variants the function *pileLettersAt* from the R/Bioconductor package *GenomicAlignments*[11] was used. The data was further filtered for variants with coverage of at least 10 reads on the transcriptome.

The DESeq2 package[12,13] was applied on the final variant set to estimate the significance of the allele-specific expression. Allele-specific expression was estimated on each heterozygous variant independently of others (i.e. without phasing the variants). For each sample, a generalized linear model was fitted with the contrast of the coverage of one allele against the

coverage of the other alleles (*condition*). Specifically, we modeled $K_{i,j}$ the number of reads of variant *i* in sample *j* as:

$$K_{i,j} \sim NB\left(s_j \times q_{i,j}, \alpha\right)$$

$$\log_2\left(q_{i,j}\right) = \beta_i^0 + \beta_i^{condition}\mathbf{x}_{i,j}^{condition}$$

Where NB is the negative binomial distribution; the dispersion parameter α was fixed for all variants to $\alpha = 0.05$, which is approximately the average dispersion over all samples based on the gene-wise analysis; s_j is the size factor of each condition; β_i^0 is the intercept parameter for variant *i*. The value of $\mathbf{x}_{i,j}^{condition}$ is 1 for the alternative alleles and 0 otherwise. The resulting $\beta_i^{condition}$ represents the $\log_2$-fold changes for the alternative allele against the reference allele. The independent filtering by DESeq2 was disabled (*independentFiltering=FALSE*) to keep the coverage outliers among the results. To classify a variant as mono-allelically expressed a cutoff of $\left|\beta_i^{condition}\right| \geq 2$ was used. This corresponds to an allele frequency ≥ 0.8.

Mass spectrometric sample preparation

Mass spectrometric sample preparation was done as described earlier[18]. Briefly, cells were lysed in SDC lysis buffer (1% sodium deoxycholate, 10 mM TCEP, 40 mM CAA, 100 mM Tris pH 8.5), boiled for 10 min at 95ºC, sonicated and diluted 1:1 with water for LysC and trypsin digestion. The dilution buffer contained appropriate amounts of proteolytic enzyme to ensure a ratio of 1:50 (µg enzyme / µg protein). Digestion was performed at 37°C overnight. Peptides were acidified, loaded on SDB-RPS (poly-styrenedivinylbenzene) material and eluted. Eluted peptides were collected in autosampler vials and dried using a SpeedVac centrifuge (Eppendorf, Concentrator plus, 5305 000.304). Peptides were resuspended in buffer A* (2% ACN, 0.1% TFA) and were sonicated (Branson Ultrasonics, Ultrasonic Cleaner Model 2510).

Mass spectrometric data acquisition

2 µg of peptides per sample were loaded for 100 min gradients separated on a 50 cm column with 75 µm inner diameter in-house packed with 1.9 µm C18 beads (Dr. Maisch GmbH). Reverse phase chromatography was performed at 50ºC with an EASY-nLC 1000 ultra-high pressure system (Thermo Fisher Scientific) coupled to the Q Exactive HF[19] mass spectrometer (Thermo Fisher Scientific) via a nanoelectrospray source (Thermo Fisher Scientific). Peptides were loaded in buffer A (0.1% volume/volume formic acid) and eluted with a nonlinear gradient. Operational parameters were real-time monitored by the SprayQC software[20]. Raw files were analysed by the software MaxQuant[21] (version 1.5.3.2) and peak lists were searched against the Homo sapiens Uniprot FASTA database (Version 2014/4) and a common contaminants database (247 entries) by the Andromeda search engine[22]. Label-free quantification was done using the MaxLFQ algorithm[23] (for detailed parameters see **Supplementary Table 5**) integrated into MaxQuant.

Processing of proteome intensities

The LFQ intensities and gene names were extracted for 6,566 protein groups from the MaxQuant output file *proteinGroups.txt*. For protein groups with more than one member, the first member was chosen to represent the group as single protein with a distinct gene name (similar to earlier studies[24]). MaxLFQ intensities of 0 actually represent non-quantified peaks and were therefore replaced with missing values (NA). The 10 samples that had a frequency of missing values higher than 50% were considered bad quality and discarded. Furthermore, proteins were discarded because they had no gene name assigned (n=198), were not the most abundant among their duplicates (n=295), were not expressed in any sample (n=93), because their 95th percentile was not detected (n=549), which was also considered as not expressed, analogously to RNA filtering. Finally, 5,431 proteins and 31 samples were considered for further analysis (**Supplementary Table 6**).

Computing protein fold changes and differential expression

Since the mass spectrometric measurements of all samples were done in a single run, no technical artifacts could be found with a hierarchical clustering. Protein differential expression for each patient compared to the others was tested using moderated T-test approach as implemented in the R/Bioconductor limma package[25]. The transcriptome covariates for sex and HOX effects were used in the linear model for normalization.

Metabolomics

Blood levels of metabolites of the proline pathway and urea cycle were determined as part of a non-targeted metabolomics experiment on 143 patients (including #80256) with mitochondrial diseases and 97 healthy controls. We used a metabolomics platform that has been established by Metabolon Inc. and is based mass spectrometry coupled to liquid (LC-MS/MS). Sample preparation, analytical protocols, identification of metabolites, and processing of the raw ion counts have been described in detail previously[26–28].

Briefly, plasma samples, which were stored at -80°C prior to analysis, were thawed on ice. For metabolite extraction and protein precipitation, 475 µL methanol, containing four recovery standards to monitor the extraction efficiency, were added to 100 µL of the plasma. After centrifugation, the supernatant was split into 4 aliquots of 100 µL each onto two 96-well microplates. The first 2 aliquots were used for LC-MS/MS analysis in positive and negative electrospray ionization mode. Two further aliquots were kept as a reserve. The extracts were dried on a TurboVap 96 (Zymark, Sotax, Lörrach, Germany). Prior to LC-MS/MS in positive ion mode, the samples were reconstituted with 50 µl 0.1% formic acid. Whereas samples analyzed in negative ion mode were reconstituted with 50 µl 6.5 mM ammonium bicarbonate, pH 8.0. Reconstitution solvents for both ionization modes contained internal standards that allowed monitoring of instrument performance and also served as retention reference markers. To minimize human error, liquid handling was performed on a Hamilton Microlab STAR robot (Hamilton Bonaduz AG, Bonaduz, Switzerland).

LC-MS/MS analysis was performed on a linear ion trap LTQ XL mass spectrometer (Thermo Fisher Scientific GmbH, Dreieich, Germany) coupled with a Waters Acquity UPLC system (Waters GmbH, Eschborn, Germany). Two separate columns (2.1 x 100 mm Waters BEH C18, 1.7 µm particle-size) were used either for acidic (solvent A: 0.1% formic acid in water, solvent

B: 0.1% formic acid in methanol) and or for basic (A: 6.5 mM ammonium bicarbonate, pH 8.0, B: 6.5 mM ammonium bicarbonate in 95% methanol) mobile phase conditions, optimized for positive and negative electrospray ionization, respectively. After injection of the sample extracts, the columns were developed in a gradient of 99.5% A to 98% B over an 11 min run time at 350 µL/min flow rate. The eluent flow was directly run through the ESI source of the LTQ XL mass spectrometer. The mass spectrometer analysis alternated between MS and data-dependent MS/MS scans using dynamic exclusion and the scan range was from 80-1000 m/z.

Metabolites were identified by Metabolon, Inc. from the LC-MS/MS data by automated multiparametric comparison with a proprietary library, containing retention times, m/z ratios, and related adduct fragment spectra.

To account for instrument inter-day differences, the raw ion counts detected for each metabolite were divided by their median per run-day. Furthermore, a log transformation of base 10 was applied as measured metabolite levels mostly follow a log-normal distribution.

Transduction and Transfection

Overexpression of *TIMMDC1* in fibroblast cell lines was performed by lentivirus-mediated expression of the full-length *TIMMDC1* cDNA (DNASU Plasmid Repository) using the ViraPower HiPerform Lentiviral TOPO Expression Kit (Thermo Fisher Scientific)[29]. *TIMMDC1* cDNA was cloned into the pLenti6.3/V5-TOPO expression vector and cotransfected into 293FT cells with the packaging plasmid mix using Lipofectamine 2000. After 24 h, the transfection mix was replaced with high glucose DMEM supplemented with 10% FBS. After further 72 h, the viral particle containing supernatant was collected and used for transduction of the fibroblast cell lines. Selection of stably expressing cells was performed using 5 µg/mL Blasticidin (Thermo Fisher Scientific) for 2 weeks.

Immunoblotting

Total fibroblast cell lysates were subjected to whole protein quantification, separated on 4-12% precast gels (Lonza) by SDS-PAGE electrophoresis and semi-dry transferred to PVDF membranes (GE Healthcare Life Sciences). The membranes were blocked in 5% non-fat milk (Bio Rad) in TBS-T for 1 h and immunoblotted using primary antibodies against CLPP (Abcam, ab56455), MCOLN1 (Abcam, ab28508), NDUFA13 (Abcam, ab110240), NDUFB3 (Abcam, ab55526), NDUFB8 (Abcam, ab110242), TIMMDC1 (Abcam, ab171978), and UQCRC2 (Abcam, ab14745) for 1 h at RT or ON at 4°C. Signals were detected by incubation with HRP-conjugated goat anti-rabbit and goat anti-mouse secondary antibodies (Jackson Immuno Research Laboratories) for 1 h and visualization using ECL (GE Healthcare Life Sciences).

Blue native PAGE (BN-PAGE)

Fresh fibroblast cell pellets were resuspended in PBS supplemented with 0.25 mM PMSF and 10 U/mL DNAse I and solubilized using 2 mg digitonin/mg protein. The mixture was incubated on ice for 15 min followed by addition of 1 mL PBS and subsequent centrifugation for 10 min at 10000 g and 4°C. The pellet was resuspended in 1x MB (750 mM ε-aminocaproic acid, 50 mM bis-Tris, 0.5 mM EDTA, pH 7.0) and subjected to whole protein quantification.

Membrane proteins were solubilized at a protein concentration of 2 µg/µL using 0.5% (v/v) *n*-dodecyl-β-d-maltoside (DDM) for 1 h on ice and centrifuge for 30 min at 10000 g at 4°C. The supernatant was recovered and whole protein amount was quantified. Serva Blue G (SBG) was added to a final concentration of 0.25% (v/v) and 60 µg protein were loaded on NativePAGE 4-16% Bis-Tris gels (Thermo Fisher Scientific). Anode buffer contained 50 mM Bis-Tris, pH 7.0, blue cathode buffer contained 15 mM Bis-Tris, 50 mM Tricine, pH 7.0, 0.02% SBG. Electrophoresis was started at 40 V for 30 min and continued at 130 V until the front line proceeded 2/3 of the gel. Subsequently, blue cathode buffer was replaced by clear cathode buffer not containing SBG (15 mM Bis-Tris, 50 mM Tricine, pH 7.0). Proteins were wet transferred to PVDF membranes and immunoblotted using primary antibodies against NDUFB8 to visualize complex I and UQCRC2 to visualize complex III.

Proline supplementation growth assay

We modified a method established earlier30. For the comparative growth assay, equal number of cells (n=250) from patient and control were seeded in 96-well plates and cultured in DMEM containing 10% of either normal or dialyzed FBS. Medium with normal FBS contains small molecules, whereas medium with dialyzed FBS is free of molecules with a molecular weight smaller than 10,000 mw (Proline-free medium). To confirm the effect of Proline deprivation, DMEM containing dialyzed FBS was supplemented with 100 µM L-Proline to rescue the growth defect. After paraformaldehyde fixation, nuclei were stained with 4',6-diamidino-2-phenylindole (DAPI) and cell number was determined using a Cytation3 automated plate reader (BioTek, USA).

Cellular ROS production

Intensity of hydroethidine (HEt) oxidation products as a measure of cellular ROS production was quantified in living skin fibroblasts using epifluorescence microscopy as described previously[31].

Methods-only References

1. Mayr, J. A. *et al.* Lack of the mitochondrial protein acylglycerol kinase causes sengers syndrome. *Am. J. Hum. Genet*. **90,** 314–320 (2012).

2. Li, H. & Durbin, R. Fast and accurate short read alignment with Burrows-Wheeler transform. *Bioinformatics* **25,** 1754–1760 (2009).

3. Li, H. A statistical framework for SNP calling, mutation discovery, association mapping and population genetical parameter estimation from sequencing data. *Bioinformatics* **27,** 2987–2993 (2011).

4. Li, H. *et al.* The Sequence Alignment/Map format and SAMtools. *Bioinformatics* **25,** 2078–2079 (2009).

5. McLaren, W. *et al.* Deriving the consequences of genomic variants with the Ensembl API

and SNP Effect Predictor. *Bioinformatics* **26,** 2069–2070 (2010).

6. Eilbeck, K. *et al*. The Sequence Ontology: a tool for the unification of genome annotations. *Genome Biol*. **6,** R44 (2005).

7. Lek, M. *et al*. *Analysis of protein-coding genetic variation in 60,706 humans*. *bioRxiv* (Cold Spring Harbor Labs Journals, 2015). doi:10.1101/030338

8. Haack, T. B. *et al*. ELAC2 mutations cause a mitochondrial RNA processing defect associated with hypertrophic cardiomyopathy. *Am. J. Hum. Genet.* **93,** 211–223 (2013).

9. Dobin, A. *et al.* STAR: Ultrafast universal RNA-seq aligner. *Bioinformatics* **29,** 15–21 (2013).

10. Hsu, F. *et al.* The UCSC Known Genes. *Bioinformatics* **22,** 1036–1046 (2006).

11. Lawrence, M. *et al*. Software for Computing and Annotating Genomic Ranges. *PLoS Comput. Biol.* **9,** e1003118 (2013).

12. Anders, S. & Huber, W. DESeq: Differential expression analysis for sequence count data. *Genome Biol.* **11,** R106 (2010).

13. Love, M. I., Huber, W. & Anders, S. Moderated estimation of fold change and dispersion for RNA-seq data with DESeq2. *Genome Biol.* **15,** 550 (2014).

14. HOCHBERG, Y. A sharper Bonferroni procedure for multiple tests of significance. *Biometrika* **75,** 800–802 (1988).

15. Li, Y. I., Knowles, D. A. & Pritchard, J. K. LeafCutter: Annotation-free quantification of RNA splicing. *bioRxiv* 044107 (2016). doi:10.1101/044107

16. Harrow, J. *et al.* GENCODE: The reference human genome annotation for The ENCODE Project. *Genome Res.* **22,** 1760–1774 (2012).

17. Pervouchine, D. D., Knowles, D. G. & Guig, R. Intron-centric estimation of alternative splicing from RNA-seq data. *Bioinformatics* **29,** 273–274 (2013).

18. Kulak, N. A., Pichler, G., Paron, I., Nagaraj, N. & Mann, M. Minimal, encapsulated proteomic-sample processing applied to copy-number estimation in eukaryotic cells. *Nat. Methods* **11,** 319–324 (2014).

19. Scheltema, R. A. *et al.* The Q Exactive HF, a Benchtop mass spectrometer with a pre-filter, high-performance quadrupole and an ultra-high-field Orbitrap analyzer. *Mol. Cell. Proteomics* **13,** 3698–708 (2014).

20. Scheltema, R. A. & Mann, M. SprayQc: A Real-Time LC-MS/MS quality monitoring system to maximize uptime using off the shelf components. *J. Proteome Res.* **11,** 3458–3466 (2012).

21. Cox, J. & Mann, M. MaxQuant enables high peptide identification rates, individualized p.p.b.-range mass accuracies and proteome-wide protein quantification. *Nat. Biotechnol.* **26,** 1367–72 (2008).

22. Cox, J. *et al.* Andromeda: A peptide search engine integrated into the MaxQuant environment. *J. Proteome Res.* **10,** 1794–1805 (2011).

23. Cox, J., Hein, M. Y., Luber, C. a & Paron, I. Accurate proteome-wide label-free quantification by delayed normalization and maximal peptide ratio extraction, termed MaxLFQ. *Mol. Cell.* … **13,** 2513–2526 (2014).

24. Cheng, Z. *et al.* Differential dynamics of the mammalian mRNA and protein expression response to misfolding stress. *Mol. Syst. Biol.* **12,** 855–855 (2016).

25. Ritchie, M. E. *et al.* Limma powers differential expression analyses for RNA-sequencing and microarray studies. *Nucleic Acids Res.* **43,** e47 (2015).

26. Evans, A. M., DeHaven, C. D., Barrett, T., Mitchell, M. & Milgram, E. Integrated, nontargeted ultrahigh performance liquid chromatography/electrospray ionization tandem mass spectrometry platform for the identification and relative quantification of the small-molecule complement of biological systems. *Anal. Chem.* **81,** 6656–6667 (2009).

27. Dehaven, C. D., Evans, A. M., Dai, H. & Lawton, K. A. Organization of GC/MS and LC/MS metabolomics data into chemical libraries. *J. Cheminform.* **2,** (2010).

28. Shin, S.-Y. *et al.* An atlas of genetic influences on human blood metabolites. *Nat. Genet.* **46,** 543–50 (2014).

29. Van Haute, L. *et al.* Deficient methylation and formylation of mt-tRNAMet wobble cytosine in a patient carrying mutations in NSUN3. *Nat. Commun.* **7,** 12039 (2016).

30. Baumgartner, M. R. *et al.* Hyperammonemia with reduced ornithine, citrulline, arginine and proline: a new inborn error caused by a mutation in the gene encoding delta(1)-pyrroline-5-carboxylate synthase. *Hum. Mol. Genet.* **9,** 2853–8 (2000).

31. Forkink, M., Smeitink, J. a M., Brock, R., Willems, P. H. G. M. & Koopman, W. J. H. Detection and manipulation of mitochondrial reactive oxygen species in mammalian cells. *Biochim. Biophys. Acta* **1797,** 1034–44 (2010).

Acknowledgements

We are grateful to the participating families. Further we thank Dr. Lina Florentin for providing DNA samples of the parents of #35791. This study was supported by the German Bundesministerium für Bildung und Forschung (BMBF) through the E-Rare project GENOMIT (01GM1603 and 01GM1207, HP and TM, FWF I 920-B13 for JAM, and J41J11000420001 for DG), through the Juniorverbund in der Systemmedizin “mitOmics” (FKZ 01ZX1405C, TBH, JG), and the DZHK (German Centre for Cardiovascular Research, LSK, TM). The study was

furthermore supported by the Deutsche Forschungsgemeinschaft (German Research Foundation) within the framework of the Munich Cluster for Systems Neurology (EXC 1010 SyNergyDFG, TM) and a Fellowship through the Graduate School of Quantitative Biosciences Munich (QBM) supports DMB. HP, VT, and JAM are supported by EU FP7 Mitochondrial European Educational Training Project (317433). HP and JG are supported by EU Horizon2020 Collaborative Research Project SOUND (633974). RWT is supported by a Wellcome Trust Strategic Award (096919/Z/11/Z) and the MRC Centre for Neuromuscular Diseases (G0601943). DG is supported by Telethon-Italy (GGP15041). We thank the Pierfranco and Luisa Mariani Foundation and the Cell lines and DNA Bank of Paediatric Movement Disorders and Mitochondrial Diseases of the Telethon Genetic Biobank Network (GTB09003).

Author contributions

Project planning: T.M., J.G., H.P. Experimental design: H.P. Review of phenotypes, sample collection and biochemical analysis: C.L., B.F., A.D., V.T., A.L., D.G., R.T., D.G., J.A.M., A.R., P.F., F.D., and T.M. Investigation L.S.K., D.M.B., and C.M. Data curation and analysis: L.S.K., D.M.B., C.M., T.M.S., and H.P. Cell biology experiments: L.S.K., R.K., A.I., C.T., E.K., and B.R. Exome, genome, and RNA sequencing; L.S.K., R.K., E.G., T.S., P.L. and T.M.S. Exome analysis: L.S.K., R.K.,T.B.H., and H.P. Quantitative proteomics: L.S.K. and G.P. Metabolomic studies: L.S.K., G.K., A.A., and J.A. Manuscript writing: L.S.K., D.M.B., C.M., G.P., J.G., and H.P. Visualization L.S.K., D.M.B., and C.M. Critical revision of the manuscript: all authors.

Competing financial interests

The authors declare that they have no competing interests.

Materials & Correspondence

Correspondence and material requests should be addressed to:

Holger Prokisch (prokisch@helmholtz-muenchen.de) or Julien Gagneur (gagneur@in.tum.de).

Supplemental tables and codes are available online at http://i12g-gagneurweb.informatik.tu-muenchen.de/public/paper/mitoMultiOmics

Figure Legends

Figure 1: Strategy for genetic diagnosis using RNA-seq

The approach we followed started with RNA sequencing of fibroblasts from unsolved WES patients. Three strategies to facilitate diagnosis were pursued: Detection of aberrant expression (i.e. depletion), aberrant splicing (i.e. exon creation) and mono-allelic expression of the alternative allele (i.e. A as alternative allele). Candidates were validated by proteomic measurements, lentiviral transduction of the wildtype (wt) allele or, in particular cases, by specific metabolic supplementation.

Figure 2: RNA expression outlier detection and validation

(a) Aberrantly expressed genes (Hochberg corrected *P*-value < 0.05 and |Z-score| > 3) for each patient fibroblasts.

(b) Gene-wise RNA expression volcano plot of nominal *P*-values (- $\log_{10}$ *P*-value) against Z-scores of the patient #35791 compared against all other fibroblasts. Absolute Z-scores greater than 5 are plotted at ±5, respectively.

(c) Same as (b) for patient #73804.

(d) Sample-wise RNA expression is ranked for the genes *TIMMDC1* (top) and *MGST1* (bottom). Samples with aberrant expression for the corresponding gene are highlighted in red (#73804, #35791, and #66744).

(e) Gene-wise comparison of RNA and protein fold changes of patient #35791 against all other fibroblast cell lines. Subunits of the mitochondrial respiratory chain complex I are highlighted (red squares). Reliably detected proteins that were not detected in this sample are shown separately with their corresponding RNA fold changes (points below solid horizontal line).

(f) Western blot of TIMMDC1, NDUFA13, NDUFB3, and NDUFB8 protein in three fibroblast cell lines without (#62346, #91324, #NHDF) and three with a variant in *TIMMDC1* (#35791, #66744, #96687), and fibroblasts re-expressing *TIMMDC1* ("-T") (#35791-T, #66744-T, #96687-T). UQCRC2 was used as loading control. MW, molecular weight; CI, complex I subunit; CIII, complex III subunit.

(g) Blue native PAGE blot of the control fibroblasts re-expressing *TIMMDC1* (NHDF-T), the control fibroblasts (NHDF), patient fibroblasts (#96687), and patient fibroblast re-expressing *TIMMDC1* (#96687-T). Immunodecoration for complex I and complex III was performed using NDUFB8 and UQCRC2 antibodies, respectively. CI, complex I subunit; CIII, complex III subunit.

Figure 3: Aberrant splicing detection and quantification

(a) Aberrant splicing events (Hochberg corrected *P*-value < 0.05) for all fibroblasts.

(b) Aberrant splicing events (n=173) grouped by their splicing category in undiagnosed patients (n=47).

(c) *CLPP* Sashimi plot of exon skipping and truncation events in affected and unaffected fibroblasts (red and orange, respectively). The RNA coverage is given as the $\log_{10}$ RPKM-value and the number of split reads spanning the given intron is indicated on the exon-connecting lines. At the bottom the gene model of the RefSeq annotation is depicted. The aberrantly spliced exon is colored in red.

(d) Same as in (c) for *TIMMDC1*. At the bottom the newly created exon is depicted in red within the RefSeq annotation track.

(e) Coverage tracks (light red) for patients #35791, #66744, and #91324 based on RNA and whole genome sequencing. For patient #91324 only WGS is available. The homozygous SNV c.596+2146A>G is present in all coverage tracks (vertical orange bar). The top tracks show the genomic annotation: genomic position on chromosome 3, DNA sequence, amino acid translation (grey, stop codon in red), the RefSeq gene model (blue line), the predominant additional exon of *TIMMDC1* (blue rectangle), and the SNV annotation of the 1000 Genomes Project (each black bar represents one variant).

(f) Percent spliced in (Ψ) distribution for different splicing classes and genes. Top: Histogram giving the genome-wide distribution of the 3' and 5' Ψ-values based on all reads over all samples. Middle: The shaded horizontal bars represent the densities (black for high density) of the background, weak and strong splicing class, respectively (Methods). Bottom: Ψ-values of the predominant donor and acceptor splice sites of genes with private splice sites (i.e found dominant in at most two samples) computed over all other samples.

Figure 4: Detection and validation of mono-allelic expression of rare variants

(a) Distribution of heterozygous single nucleotide variants (SNVs) across samples for different consecutive filtering steps. Heterozygous SNVs detected by exome sequencing (black), SNVs with RNA-seq coverage of at least 10 reads (gray), SNVs where the alternative allele is mono-allelically expressed (alternative allele frequency > 0.8 and Benjamini-Hochberg corrected *P*-value < 0.05, blue), and the rare subset of those (ExAC minor allele frequency < 0.001, red).

(b) Fold change between alternative (ALT+1) and reference (REF+1) allele read counts for the patient #80256 compared to total read counts per SNV within the sample. Points are colored according to the groups defined in (a).

(c) Gene-wise comparison of RNA and protein fold changes of the patient #80256 against all other patients' fibroblasts. The position of the gene *ALDH18A1* is highlighted. Reliably detected proteins that were not detected in this sample are shown separately with their corresponding RNA fold changes (points below solid horizontal line).

(d) Relative intensity for metabolites of the proline biosynthesis pathway (inlet) for the patient #80256 and 16 healthy controls of matching age. Equi-tailed 95% interval (whiskers), 25th, 75th percentile (boxes) and median (bold horizontal line) are indicated. Data points belonging to the patient are highlighted (red circles and triangles, if Student's *t*-test *P*-value < 0.05).

(e) Cell counts under different growth conditions for the normal human dermal fibroblast (NHDF) and patient #80256. Both fibroblasts were grown in fetal bovine serum (FBS), dialyzed FBS (without proline) and dialyzed FBS with proline added. Boxplot as in (d). *P*-values are based on a two-sided Wilcoxon test.

(f) Intron retention for *MCOLN1* in patient #62346. Tracks from top to bottom: genomic position on chromosome 19, amino acid translation (red for stop codons), RefSeq gene model, coverage of whole exome sequencing of patient #62346, RNA-seq based coverage for patients #62346 and #85153 (red and orange shading, respectively). SNVs are indicated by non-reference colored bars with respect to the corresponding reference and alternative nucleotide.

Figure 5: Graphical summary

(a) Discovery and validation of hidden variant effects in *TIMMDC1*, *MGST1*, *CLPP*, *ALDH18A1*, and *MCOLN1* by RNA sequencing. The median number (± median absolute deviation) of candidate genes is given per detection strategies. Dotted check, not significant.

(b) Schematic representation of variant causing splicing defects for TIMMDC1 (top, new exon red box), CLPP (middle, exon skipping and truncation), and MCOLN1 (bottom, intron retention). Variants are depicted by a red star.

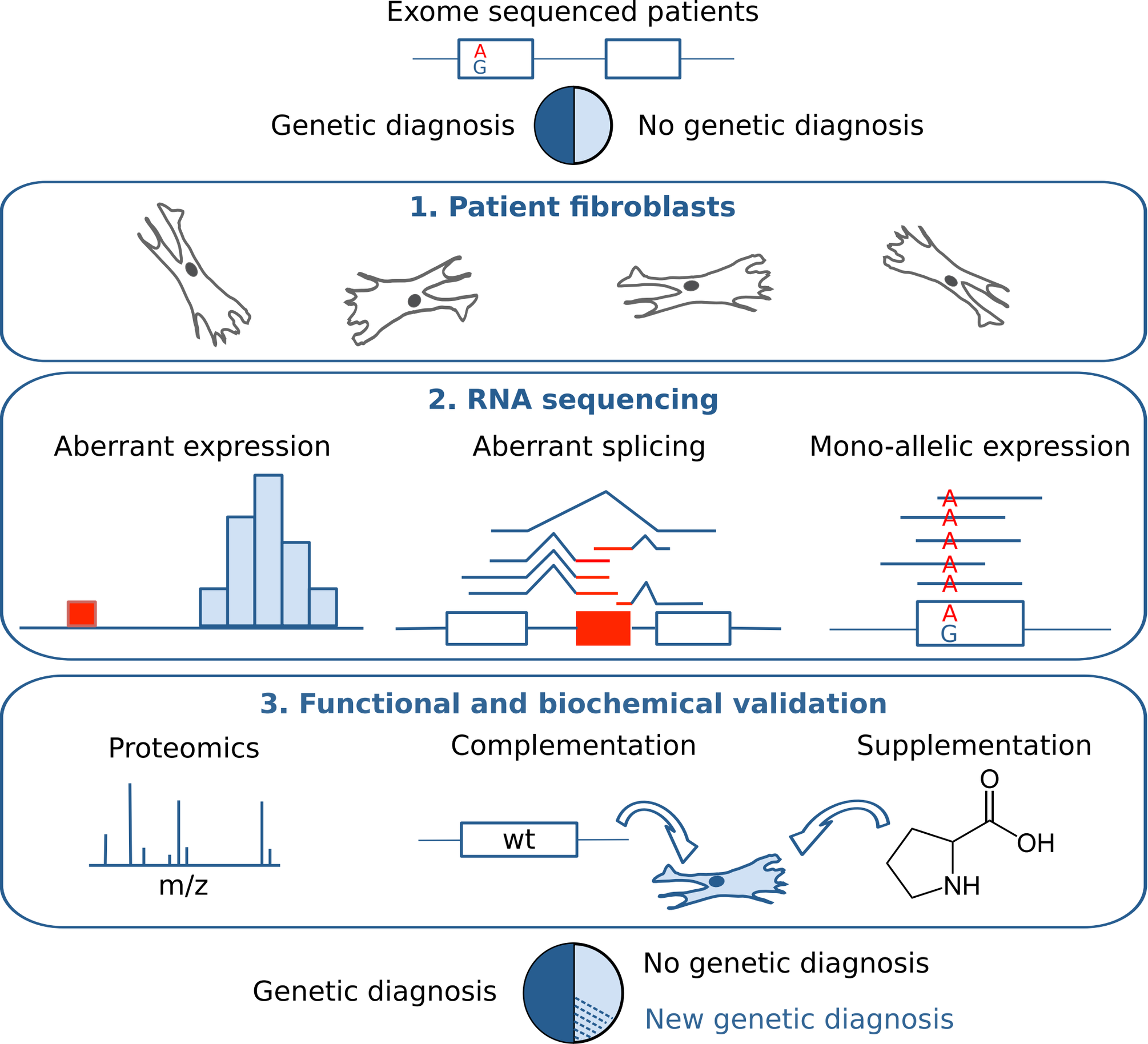
Exome sequenced patients
A
G
Genetic diagnosis
No genetic diagnosis
1. Patient fibroblasts
2. RNA sequencing
Aberrant expression
Aberrant splicing
Mono-allelic expression
A
A
A
A
A
A
G
3. Functional and biochemical validation
Proteomics
Complementation
Supplementation
m/z
wt
O
OH
NH
Genetic diagnosis
No genetic diagnosis
New genetic diagnosis

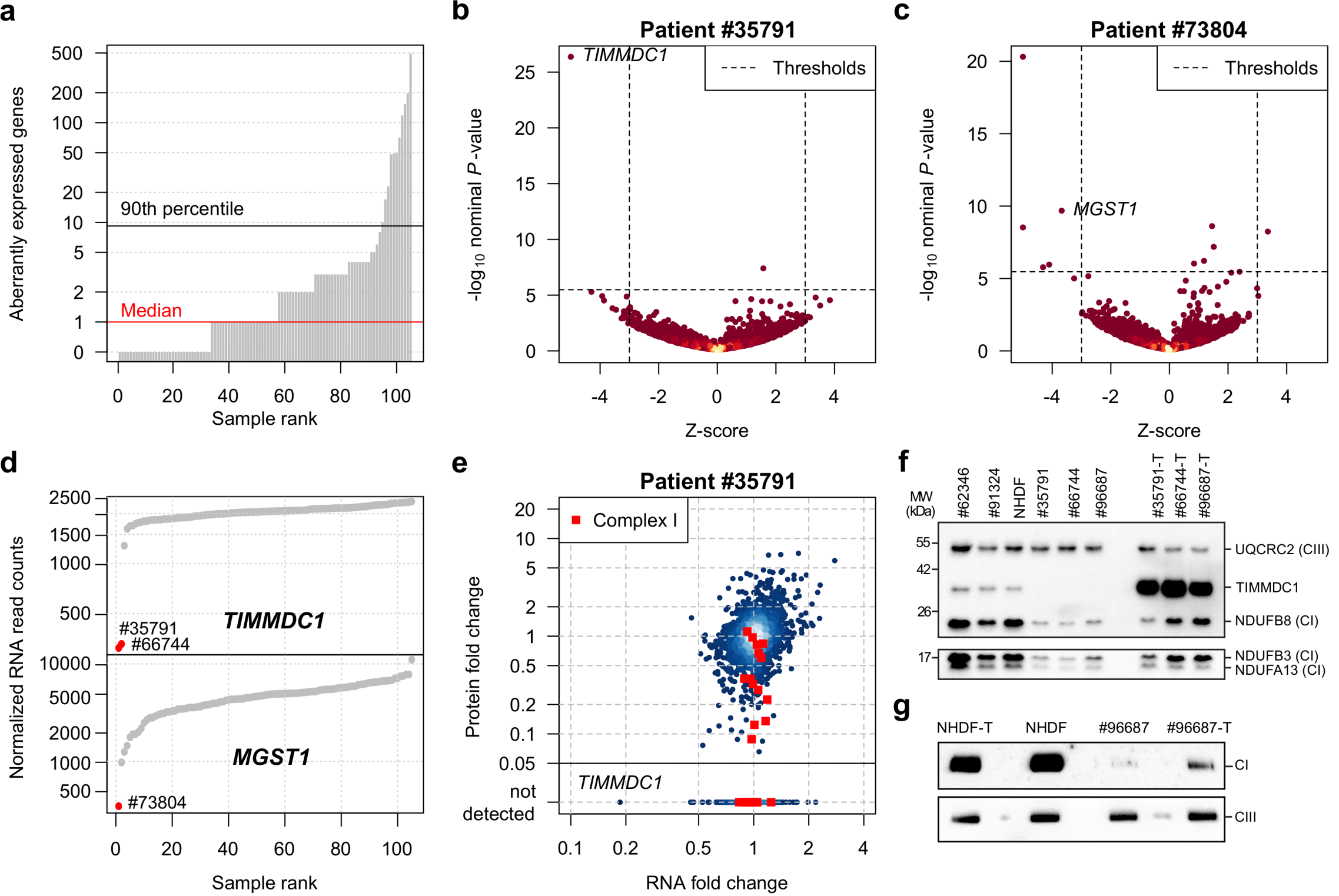
a
Aberrantly expressed genes
500
200
100
50
20
10
5
2
1
0
90th percentile
Median
0
20
40
60
80
100
Sample rank
b
Patient #35791
TIMMDC1
Thresholds
-log10 nominal P-value
25
20
15
10
5
0
-4
-2
0
2
4
Z-score
c
Patient #73804
Thresholds
MGST1
-log10 nominal P-value
20
15
10
5
0
-4
-2
0
2
4
Z-score
d
Normalized RNA read counts
2500
1500
1000
500
#35791
#66744
TIMMDC1
10000
5000
2000
1000
500
MGST1
#73804
0
20
40
60
80
100
Sample rank
e
Patient #35791
Complex I
Protein fold change
20
10
5
2
1
0.5
0.2
0.1
0.05
not detected
TIMMDC1
0.1
0.2
0.5
1
2
4
RNA fold change
f
MW (kDa)
#62346
#91324
NHDF
#35791
#66744
#96687
#35791-T
#66744-T
#96687-T
55
42
26
17
UQCRC2 (CIII)
TIMMDC1
NDUFB8 (CI)
NDUFB3 (CI)
NDUFA13 (CI)
g
NHDF-T
NHDF
#96687
#96687-T
CI
CIII

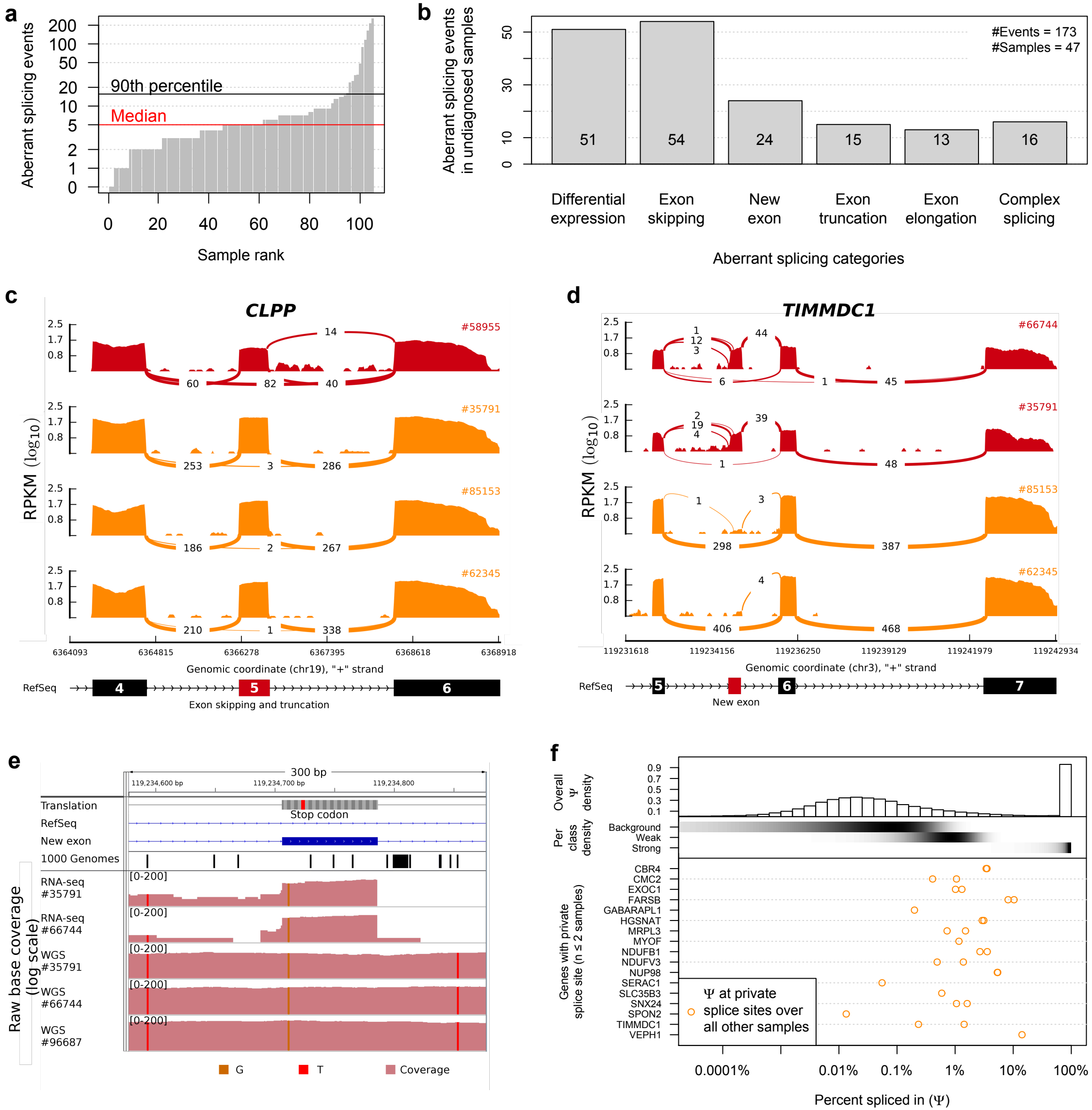
a
Aberrant splicing events
200
100
50
20
10
5
2
1
0
90th percentile
Median
0
20
40
60
80
100
Sample rank
b
Aberrant splicing events in undiagnosed samples
#Events = 173
#Samples = 47
51
54
24
15
13
16
Differential expression
Exon skipping
New exon
Exon truncation
Exon elongation
Complex splicing
Aberrant splicing categories
c
CLPP
#58955
#35791
#85153
#62345
RPKM (log10)
Genomic coordinate (chr19), "+" strand
RefSeq
Exon skipping and truncation
d
TIMMDC1
#66744
#35791
#85153
#62345
Genomic coordinate (chr3), "+" strand
RefSeq
New exon
e
300 bp
Translation
Stop codon
RefSeq
New exon
1000 Genomes
RNA-seq #35791
RNA-seq #66744
WGS #35791
WGS #66744
WGS #96687
Raw base coverage (log scale)
G
T
Coverage
f
Overall Ψ density
Per class density
Background
Weak
Strong
Genes with private splice site (n ≤ 2 samples)
CBR4
CMC2
EXOC1
FARSB
GABARAPL1
HGSNAT
MRPL3
MYOF
NDUFB1
NDUFV3
NUP98
SERAC1
SLC35B3
SNX24
SPON2
TIMMDC1
VEPH1
Ψ at private splice sites over all other samples
0.0001%
0.01%
0.1%
1%
10%
100%
Percent spliced in (Ψ)

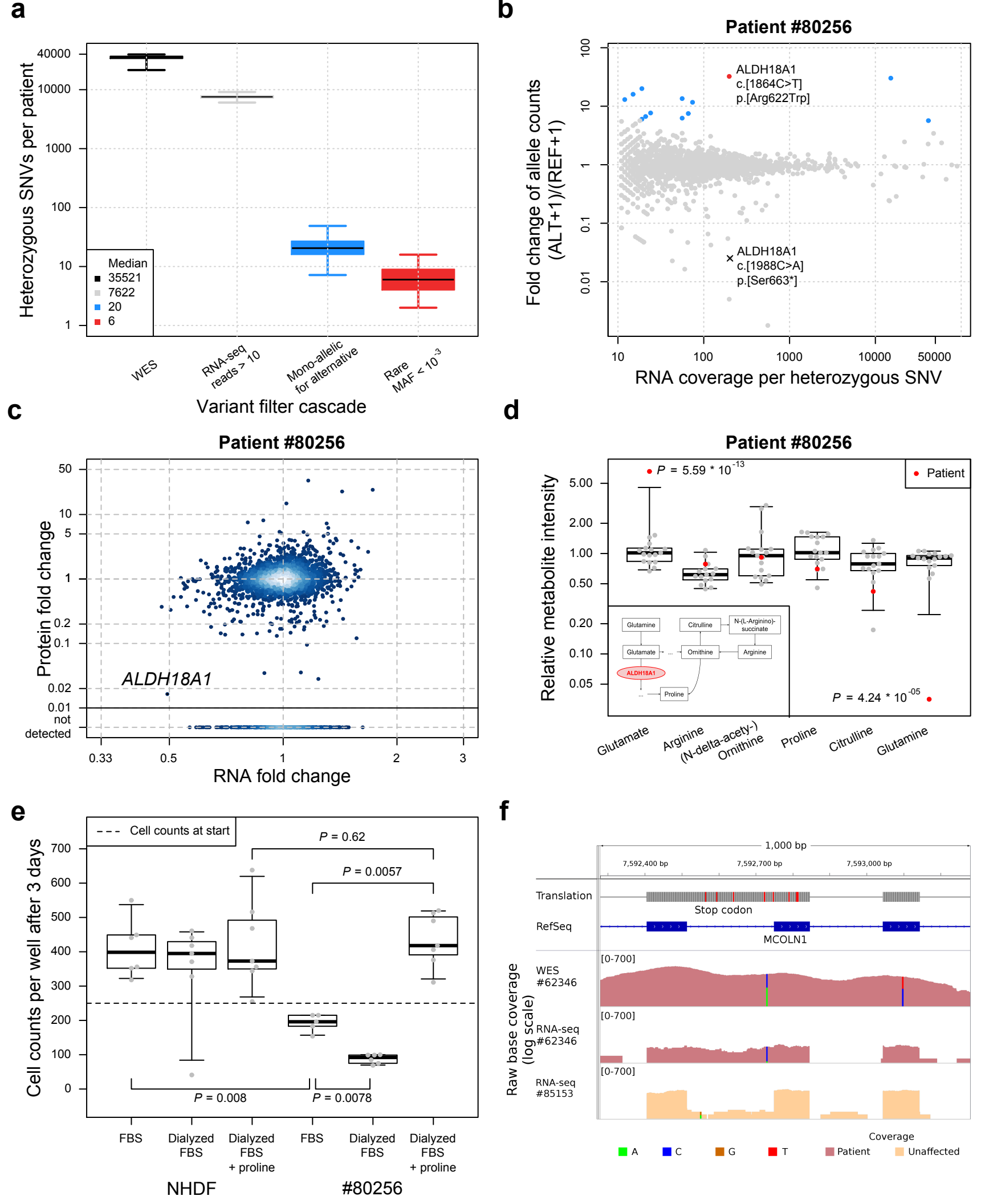
a
Heterozygous SNVs per patient
40000
10000
1000
100
10
1
Median
35521
7622
20
6
WES
RNA-seq reads > 10
Mono-allelic for alternative
Rare MAF < 10^-3
Variant filter cascade
b
Patient #80256
Fold change of allele counts (ALT+1)/(REF+1)
100
10
1
0.1
0.01
ALDH18A1
c.[1864C>T]
p.[Arg622Trp]
ALDH18A1
c.[1988C>A]
p.[Ser663*]
10
100
1000
10000
50000
RNA coverage per heterozygous SNV
c
Patient #80256
Protein fold change
50
10
5
1
0.2
0.1
0.02
0.01
not detected
ALDH18A1
0.33
0.5
1
2
3
RNA fold change
d
Patient #80256
Relative metabolite intensity
P = 5.59 * 10^-13
Patient
5.00
2.00
1.00
0.50
0.20
0.10
0.05
Glutamine
Citrulline
N-(L-Arginino)-succinate
Glutamate
Ornithine
Arginine
ALDH18A1
Proline
P = 4.24 * 10^-05
Glutamate
Arginine (N-delta-acety-) Ornithine
Proline
Citrulline
Glutamine
e
Cell counts at start
Cell counts per well after 3 days
P = 0.62
P = 0.0057
P = 0.008
P = 0.0078
700
600
500
400
300
200
100
0
FBS
Dialyzed FBS
Dialyzed FBS + proline
FBS
Dialyzed FBS
Dialyzed FBS + proline
NHDF
#80256
f
1,000 bp
7,592,400 bp
7,592,700 bp
7,593,000 bp
Translation
Stop codon
RefSeq
MCOLN1
Raw base coverage (log scale)
WES #62346
[0-700]
RNA-seq #62346
[0-700]
RNA-seq #85153
[0-700]
Coverage
A
C
G
T
Patient
Unaffected

a
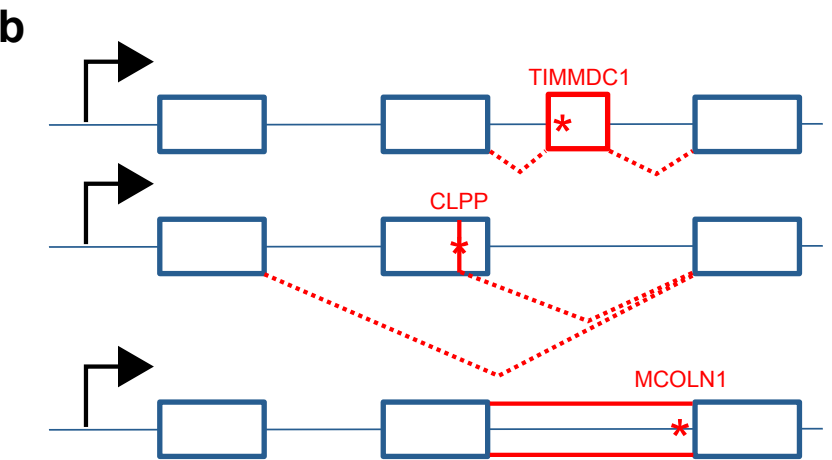
		TIMMDC1	MGST1	CLPP	ALDH18A1	MCOLN1	Candidates per sample
Detected by	Aberrant expression	✓	✓	-	✓	✓	1± 1
	Aberrant splicing	✓	-	✓	-	✓	5± 3
	Mono-allelic expression	-	-	-	✓	✓	6± 3
Validated by	Proteomics/Western blot	✓	✓	✓	✓	-	
	Complementation	✓	-	-	-	-	
	Supplementation	-	-	-	✓	-	
	Disease associated variant detecetd	✓	-	✓	✓	✓